Statistical Study of EMIC Waves and Related Proton Distributions Observed by the Arase Satellite

C.-W. Jun[1], Y. Miyoshi[1], S. Nakamura[1], M. Shoji[1], M. Kitahara[1], T. Hori[1], C. Yue[2], J. Bortnik[3], L. Lyons[3], K. Min[4], Y. Kasahara[5], F. Tsuchiya[6], A. Kumamoto[6], K. Asamura[7], I. Shinohara[7], A. Matsuoka[8], S. Imajo[8], S. Yokota[9], S. Kasahara[10], and K. Keika[10]

[1]Institute for Space-Earth Environmental Research (ISEE), Nagoya University, Nagoya, Japan

[2]Institute of Space Physics and Applied Technology, Peking University, Beijing, China

[3]AOS/UCLA, Los Angeles, USA

[4]Chungnam National University, Daejeon, Korea

[5]Kanazawa University, Kanazawa, Japan

[6]Tohoku University, Sendai, Japan

[7]ISAS/JAXA, Tokyo, Japan

[8]Kyoto University, Kyoto, Japan

[9]Osaka University, Osaka, Japan

[10]University of Tokyo, Tokyo, Japan

Corresponding author: Chae-Woo Jun (chae-woo@isee.nagoya-u.ac.jp)

Key Points:

- H- (He-) EMIC waves are observed in the morning-noon (afternoon) sector outside (inside) the plasmasphere.
- EMIC waves are generated at the magnetic equator near the threshold of proton cyclotron instability and propagate to higher latitudes.
- The energy ranges of the observed proton pitch angle scatter differ in different occurrence regions, and coincide with the resonance energy using the central EMIC wave frequency.

Abstract

We performed a statistical study of electromagnetic ion cyclotron (EMIC) wave distributions and their coupling with energetic protons in the inner magnetosphere using the Arase satellite data from May 2017 to December 2020. We investigated the energetic proton pitch-angle distributions and partial thermal pressures associated with EMIC waves using inter-calibrated proton data in the energy range of 30 eV/q-187 keV/q. With a cold plasma approximation, we computed the proton minimum resonance energies using the observed EMIC wave frequency and plasma density values. We found that the EMIC waves had left-handed polarization near the magnetic equator close to the threshold of proton cyclotron instability, and propagated to higher latitudes along the field line with polarization reversal. H-EMIC waves showed two peak occurrence regions in the morning and noon sectors at L = 7.5-9 outside the plasmasphere. The flux enhancements associated with morning side H-EMIC waves appeared at E < 1 keV/q among all pitch angles, while H-EMIC waves in the noon sector exhibited flux enhancement in field-aligned directions at E = 1-100 keV/q. He-EMIC waves showed a broad occurrence region from 12 to 20 magnetic local time at L = 5.5-8.5 inside the plasmasphere with strong flux enhancements at all pitch-angle ranges at E = 1-100 keV/q. The proton minimum resonance energy using the obtained central frequency was consistent with the observed flux enhancements at different peak occurrence regions. We conclude that the free energy sources of EMIC waves in different geomagnetic environments drive various types of EMIC waves, and they interact with energetic protons at different energy ranges.

Plain Language Summary

Electromagnetic ion cyclotron (EMIC) waves are considered to play an important role in controlling magnetospheric plasma dynamics. Specifically, EMIC wave-particle interactions can cause the loss of energetic protons and relativistic electrons in the Earth's magnetosphere, and the scattered particles precipitate into the ionosphere, creating isolated proton auroras at sub-auroral latitudes (55-65 geomagnetic latitudes). To understand the coupling of EMIC waves with energetic protons in the inner magnetosphere, we performed a statistical study of proton distributions associated with EMIC waves using a 4-year in-situ observation obtained by the Arase satellite. We observed dawn-dusk asymmetric EMIC wave distributions depending on the wavebands. We also found three significantly different regions of EMIC waves showing different characteristics. EMIC waves were inferred to be generated near the magnetic equator and propagate to higher magnetic latitudes along the field line. Furthermore, EMIC waves in different regions were proposed to interact with energetic protons at different energy ranges. The Arase satellite observations used in this study provided new insights into the dynamics of EMIC waves in the inner magnetosphere.

1 Introduction

Earth's magnetosphere consists of various plasma populations at varying energy and plasma density conditions (Borovsky and Valdivia, 2018). The plasmasphere consists of the densest (> 100/cm^3) and coldest (< 1 eV) plasma within the range of 1-4 R_E. The ring current region has a torus-like structure with the highest energy density in the inner magnetosphere (Kanekal and Miyoshi, 2021). During disturbed geomagnetic conditions, energetic plasma is transported from the magnetotail to the magnetosphere, contributing to various plasma distributions in the inner magnetosphere. This causes different types of instabilities in the generation of various plasma waves (e.g., Thorne, 2010; Miyoshi et al., 2018a).

Electromagnetic Ion Cyclotron (EMIC) waves are one of the magnetospheric plasma waves that play an important role in the loss of energetic protons and sub-relativistic, relativistic, and ultra-relativistic electrons in the outer radiation belts due to pitch-angle scattering by wave-particle interactions (Thorne, 2010; Kurita et al., 2018; Li and Hudson, 2019; Miyoshi et al., 2022). The protons scattered by EMIC wave-particle interactions precipitate into the ionosphere, causing isolated proton auroras (IPAs) at sub-auroral latitudes (55-65 geomagnetic latitudes) (Sakaguchi et al., 2007; Ozaki et al., 2018, 2021) and relativistic electrons simultaneously precipitate inside IPAs (Miyoshi et al., 2008; Shumko et al., 2022).

EMIC waves have left-handed (LH) polarizations near the wave source regions in the frequency range below the proton gyrofrequency. Because of the existence of heavy ions, the EMIC wave branch can be divided into three regimes in the dispersion relation: H-band EMIC waves, hereafter referred to as H-EMIC waves, between the proton (f_{cH}) and helium (f_{cHe}) gyrofrequencies; He-band EMIC waves, hereafter referred to as He-EMIC waves, between f_{cHe} and oxygen gyrofrequency (f_{cO}); and O-EMIC waves below f_{cO} (e.g., Kozyra et al., 1984; Chen et al., 2010).

An inverse relationship between the temperature anisotropy ($T_{\perp,p}/T_{\parallel,p}$) and parallel proton plasma beta ($\beta_{\parallel,p}$) for the proton-electron system can be derived as:

$$\frac{T_\perp}{T_\parallel} = 1 + \frac{a}{\beta_\parallel^b} \quad (1)$$

where the parameters a and b are obtained as functions of the ratio between the hot and cold proton densities. Here, $T_{\perp,p}$ and $T_{\parallel,p}$ are the perpendicular and parallel components of the proton temperature to the ambient magnetic field, $\beta_{\parallel,p} = 8\pi n_p T_{\parallel,p}/B_0^2$, where $n_p$and B_0 are the proton density and background magnetic field, respectively. Temperature anisotropy contributes to the generation of EMIC waves (Conwall et al., 1970), and the proton distributions are modified to a linear marginally stable state (i.e., relaxed state), by EMIC wave-particle interaction. Plasma kinetic theory has shown the threshold conditions of ion cyclotron anisotropy instability as the upper bound on the relaxed proton distribution (Gary & Lee, 1994, Blum et al., 2009). Several satellite-based studies have suggested that this inverse relationship of EMIC waves can help determine their generation conditions and used as a proxy for their existence (Blum et al., 2009; Lin et al, 2014; Noh et al., 2018; Yue et al., 2019). However, the parameters a and b have not yet been clearly established.

Over several decades, numerous studies have examined the spatial distribution of EMIC waves in the magnetosphere using in-situ satellite observations (e.g., Allen et al., 2015, 2016; Anderson et al., 1992a, 1992b; Halford et al., 2010; Jun et al., 2019a, 2019b, 2021; Keika et al.,

2013; Kim et al., 2016b; Usanova et al., 2012; Matsuda et al., 2018a; Min et al., 2012; Meredith et al., 2014; Nakamura et al., 2014; Park et al., 2016, 2017; Saikin et al., 2015; Vines et al., 2019; Yue et al., 2019; Wang et al., 2015, 2017). These studies also demonstrated the relationship between EMIC wave distributions and geomagnetic conditions. For example, Min et al. (2012) reported that H- and He-EMIC waves are mainly observed at 10-12 R_E in the morning sector and at 8-12 R_E in the afternoon sector, respectively, using Time History of Events and Macroscale Interactions during Substorms (THEMIS) observations. Park et al. (2017) investigated the relationship between the occurrence of EMIC waves and the interplanetary magnetic field (IMF) using THEMIS observations and reported that H-EMIC waves have a peak occurrence region in the dawn sector during the northward IMF Bz. EMIC waves become more frequent beyond the geosynchronous orbit with an increase in the solar wind dynamic pressure on the dayside of the magnetosphere (e.g., Usanova et al., 2012; Park et al., 2016). Using the Van Allen Probes observations, Jun et al. (2019a, 2019b) reported that enhanced He-EMIC waves have the highest occurrence rate in the afternoon sector inside the plasmasphere associated with energetic particle injections. A recent study using Arase and Van Allen Probe observations (Jun et al., 2021) reported that H-EMIC waves in the morning sector at L > 8 are predominant during quiet geomagnetic conditions, while He-EMIC waves peak at L ~ 6-8 in the afternoon-dusk sector with strongly enhanced wave power during the storm main phase.

Magnetospheric convection during active geomagnetic conditions transports energetic protons in the energy range of 1-100 keV from the plasma sheet to the inner magnetosphere (e.g., Ebihara and Miyoshi, 2011; Yue et al., 2017a, 2017b). Convective transportation causes temperature anisotropy, which is the free energy source for exciting EMIC waves in the afternoon sector near the plasmapause (e.g., Jun et al., 2019a; Saikin et al., 2016; Yue et al., 2019, 2020; Wang et al., 2016). Saikin et al. (2016) performed a statistical study using the Van Allen Probes and reported that an increase in the occurrence of EMIC waves tends to move from noon to the afternoon sector at L~4-6 as the AE index increases. Based on the Van Allen Probes and GOES observations, Jun et al. (2019a) reported that He-EMIC waves are mainly found in the noon-afternoon sector inside the plasmasphere associated with substorm injections.

Recently, Jun et al. (2021) reported that H-EMIC waves outside the plasmasphere in the morning sector exhibit frequencies very close to f_{cH}. The unusual high-frequency EMIC waves exhibited a narrow bandwidth and were mainly detected on the dayside of the magnetosphere outside the plasmasphere under quiet geomagnetic conditions, indicating that energetic protons alone are not sufficient for exciting EMIC waves under these conditions. Studies have suggested that warm protons with energies of < 1 keV can possibly be a free energy source for generating unusual high-frequency EMIC waves in the morning sector (Teng et al., 2019; Min et al., 2021). Asamura et al. (2021) used Arase satellite observations to demonstrate that equatorial noise can lead to the resonant heating of suprathermal protons (10-100 eV), which can subsequently generate EMIC waves near f_{cH}.

Enhanced solar wind dynamic pressure can cause proton temperature anisotropy on the dayside of the magnetosphere. (Anderson and Hamilton, 1993; McCollough et al., 2010; Yue et al., 2009, 2010, 2011). Previous studies have investigated the relationship between increasing solar wind dynamic pressure and the occurrence of EMIC waves, suggesting that this process mainly drives EMIC waves on the dayside magnetosphere (Engebretson et al., 2002; Usanova et al., 2008, 2012; Nakamura et al., 2014; Park et al., 2016; Tsurutani et al., 2016; Jun et al., 2019b).

Recent studies proposed that EMIC waves can be excited in off-equatorial source regions

at high latitudes. When the magnetosphere is compressed, the temperature anisotropy increases owing to drift-shell splitting and executing Shabansky orbits in the off-equatorial source regions at higher L-shells, exciting EMIC waves within those regions (Allen et al., 2015, 2016; McCollough et al., 2012; Vines et al., 2019).

Non-linear effects and mode conversion of EMIC waves can be possible candidate for generating EMIC waves in the magnetosphere. Recently, it has been suggested that non-linear interactions between energetic particles and EMIC waves can create a proton hill and hole in the phase space, triggering rising and falling tone EMIC emissions, respectively (Sakaguchi et al., 2013; Nakamura et al., 2016; Shoji et al., 2018, 2021). Miyoshi et al. (2019) reported that plasmaspheric EMIC waves could also be generated through mode conversion from equatorial noise.

Recent studies (Jun et al., 2019a, 2019b, 2021) have reported EMIC waves peak at different regions in the inner magnetosphere, implying that they are generated by different processes depending on the plasma environment. To understand their coupling, we performed a statistical study of the energetic proton distributions associated with EMIC waves. In this paper, we present the spatial distributions of EMIC waves as observed by the Arase satellites during 2017-2020 and compare them with the associated proton distributions. We also computed the minimum resonance energy of protons using the observed EMIC wave frequency and compared it to in-situ particle observations.

2 Observation

2.1 Instruments

The Arase satellite, which belongs to the Exploration of energization and Radiation in Geospace (ERG) project, was launched in December 2016. This satellite has an elliptical orbit with a perigee and an apogee of 400 km and 6 R_E, respectively (Miyoshi et al., 2018a). The orbital and spin periods are ~9.5 h and 8 s, respectively. The orbital inclination angle is 31˚. We used a Magnetic Field Experiment (MGF; Matsuoka et al., 2018a) to identify EMIC waves. The partial thermal pressure and pitch angle distribution for protons were obtained by a Low-Energy Particle Experiments–Ion mass Analyzer (LEPi; Asamura et al, 2018) and a Medium-Energy Particle Experiments-Ion Mass Analyzer (MEPi; Yokota et al., 2018). A High-Frequency Analyzer (HFA; Kumamoto et al., 2018), part of the Plasma Wave Experiment (PWE) (Kasahara et al., 2018a), provided the background electron density (N_e) derived from the observed upper hybrid resonance (UHR) frequency. Satellite positions, such as the magnetic local time (MLT) and magnetic latitude (MLAT) in solar magnetic coordinates, were obtained from ERG Level-2 orbit data (Miyoshi et al., 2018c). The L* values and estimated equatorial magnetic field intensity were obtained from ERG Level-3 orbit data (Miyoshi et al., 2018d) based on the Tsyganenko-Sitnov 2005 (TS05) magnetic field model (Tsyganenko and Sitnov, 2005).

2.2 Data Analysis

2.2.1 Spectral analysis of the magnetic field

We computed the dynamic spectra of the magnetic field to detect the EMIC waves in the frequency domain. The original Level-2 magnetic field data measured by the MGF instrument contained harmonic spin-tone noises, thus we applied the spin-tone reducing method of Imajo et al. (2021) to the 64 Hz magnetic field waveform dataset. To obtain clean wave signals, we subtracted the 10 s moving average magnetic field data from the original data. We then rotated the magnetic field vector into the mean-field-aligned (MFA) coordinate system (Takahashi et al., 1990) using a 32-s moving average. The x-, y-, and z-components in the MFA coordinate system are in the radial (outward), azimuthal (eastward), and parallel (northward) directions to the ambient magnetic field, respectively. Finally, using a 64-s time window (4,096 data points) and a 15-s moving window, we applied a fast Fourier transform to the rotated waveform dataset to obtain the spectral matrix of each component in time and frequency space. Thus, the frequency and time resolution of the spectral matrix were 0.0156 Hz and 15 s, respectively.

2.2.2 Energetic proton data analysis

LEPi and MEPi measured the differential flux of ions with energies of 30 eV/q - 25 keV/q and 9.6-187 keV/q, respectively. Their sampling time for three-dimensional distribution function was ~8 s. We used the nominal mode observation data from two instruments, and they retained information on the three-dimensional distribution of ion fluxes. Using three-dimensional distribution functions of protons and an 8 s spin-averaged magnetic field, we computed the pitch-angle distribution (PAD) of protons with 11.25˚ pitch-angle bins. All PAD data from LEPi and MEPi were averaged over a 1-min time window.

Before combining the PAD obtained from the two ion instruments, inter-calibration was performed to obtain continuous proton flux variations in the energy range of 30 eV/q to 187 keV/q. We computed the spin-averaged ratio between LEPi and MEPi for their overlapping energy range (8-25 keV/q), which was used inter-calibration. The ratio was averaged over a 1-day time window. Using the derived ratio, the flux of MEPi in the energy range of 25-187 keV/q was changed, while the instrument sensitivity was not necessarily constant over the entire energy range. The average and standard deviation of the ratio for the entire period (2017-2020) are 1.27 and 0.34, respectively. The combined energy range of 30 eV/q-187 keV/q for the protons was sufficient to investigate their distributions from warm plasma (> 30 eV) to ring current (~ several tens to a few hundred keV) populations (Daglis et al., 1999; Jahn et al., 2017).

The partial proton pressures in the directions perpendicular ($P_\perp$) and parallel ($P_\parallel$) to the ambient magnetic field were calculated using the energy (E) and pitch-angle (α) distributions of the differential energy flux ($J(E,\alpha)$). We used the inter-calibrated proton PAD data in the energy range of 30 eV/q-187 keV/q in the following equations (De Michelis et al., 1999; Imajo et al., 2019; Yue et al., 2018):

$$P_\perp = \pi \sum_E \sum_\alpha \sqrt{2m_p E} J(E,\alpha) sin^3\alpha \Delta E \Delta\alpha$$

$$P_\parallel = 2\pi \sum_E \sum_\alpha \sqrt{2m_p E} J(E,\alpha) cos^2\alpha \sin\alpha \, \Delta E \Delta\alpha \quad (2)$$

where m_p is the proton mass, ΔE is the energy channel width, and $\Delta\alpha$ is the pitch angle bin width (11.25˚). We then computed the temperature anisotropy ($T_\perp/T_\parallel$) using the obtained partial proton pressure, except for the small $P_\parallel$ ($P_\parallel < 0.1\ nPa$), because they became unreliable.

The parallel plasma beta ($\beta_{\parallel}$) is defined as the ratio between the parallel proton pressure and local magnetic pressure, as follows:

$$\beta_{\parallel} = 2\mu_0 P_{\parallel}/B_{local}^2 \quad (3)$$

where μ_0 is the permeability of free space.

2.2.3 Calculation of the minimum resonance energy for protons

We calculated the plasma dispersion relation for electromagnetic waves propagating in the parallel direction with respect to the ambient magnetic field in a cold plasma containing a mixture of proton, helium, and oxygen ions (Meredith et al., 2003; Stix 1962; Walker, 1993). The dispersion relation for the L-mode is defined as

$$\frac{c^2k^2}{\varpi^2} = 1 - \frac{\varpi_{pe}^2}{\varpi(\varpi+|\Omega_e|)} - \sum_{l=1}^{3}\frac{\varpi_{pl}^2}{\varpi(\varpi-\Omega_l)} \quad (4)$$

where ϖ is the angular frequency ($\varpi = 2\pi f$), ϖ_{pe} and ϖ_{pl} are the electron and proton plasma frequencies, respectively. Ω_e is the electron cyclotron frequency, and Ω_l is the ion cyclotron frequency of the l species. The suffix l denotes the ion species, with values l = 1, 2, and 3 referring to the proton, helium, and oxygen ions, respectively.

It is important to consider the ion composition ratio (H^+:He^+:O^+) in the dispersion relation of EMIC waves. The direct measurement of the ion composition ratio was not available because the minimum energy of the LEPi instrument used in this study was 30 eV. Total ion composition is highly dependent on the geomagnetic activity, particularly the geomagnetic storm phase. For example, the O^+ composition increases the total ion composition owing to a large increase in hot O^+ during the main phase of geomagnetic storms (e.g., Yue et al., 2018). However, it is not necessary to consider the influence of hot heavy ion composition on EMIC wave growth at heavy ions gyrofrequencies (Silin et al., 2011). Instead, we considered the validity of the cold ion compositions to calculate a reliable dispersion relationship for EMIC waves from previous studies (e.g., Omura et al., 2010; Pakhotin et al., 2013; Silin et al., 2011). Jun et al. (2021) has reported that the regions of peak EMIC wave occurrence have different geomagnetic preferences for their generations. H-EMIC waves are predominantly observed in the morning sector outside the plasmasphere during quiet conditions, whereas He-EMIC waves tend to be observed in the afternoon sector inside the plasmasphere during disturbed conditions (Jun et al., 2019a and 2021). To calculate the proton minimum resonance energy, we considered two empirical nominal ion compositions: H^+:He^+:O^+=0.85:0.1:0.05 under the general geomagnetic conditions for H-EMIC waves (Meredith et al., 2003), and H^+:He^+:O^+=0.97:0.02:0.01 for He-EMIC waves inside the plasmasphere (Silin et al., 2011).

For protons, the resonance condition with L-mode waves is

$$\varpi - k_{\parallel}v_{\parallel} = \frac{\Omega_p}{\gamma} \quad (5)$$

where $\gamma = (1 - v^2/c^2)^{-1/2}$ and $v^2 = v_{\perp}^2 + v_{\parallel}^2$. Using the value of k from Eq. (4) and Eq. (5) and substituting $v_{\perp} = 0$, the minimum resonance energy for protons, $E_{p,min}$, is determined by the following equation:

$$E_{p,min} = (\gamma - 1)m_p c^2. \quad (6)$$

$E_{p,min}$ was calculated using the equatorial magnetic field intensity obtained using the TS05 model for the cyclotron frequency and local background electron density for the plasma frequency.

2.3 Event selection

We collected the EMIC wave events observed by the Arase satellite in 2017-2020 based on the event selection method of Jun et al. (2019a). The selection criteria were as follows:

1. The spectral structures of EMIC waves must be observed below f_{cH} in the perpendicular magnetic field component of the dynamic spectrum.

2. The wave power and minimum duration of EMIC waves must be > 10^{-4} nT^2/Hz and 5 min, respectively.

3. The background and artificial noises that have lower degrees of polarization and coherences (< 0.5) must be excluded from the event list.

4. If the harmonic-like events are observed simultaneously, only the fundamental wave structures were considered as an individual event.

As O-EMIC waves are difficult to distinguish from other ultra-low frequency emissions because of their extremely low frequency in the region beyond L*>4 in the magnetosphere, we disregarded them in this study. Therefore, we only categorized the selected EMIC waves based on the equatorial ion cyclotron frequencies, i.e., H- and He-EMIC waves.

To determine $E_{p,min}$ associated with the observed EMIC waves, we collected the frequency of the peak wave power within the selected frequency boundary as the central frequency. Based on the wave analysis of Jun et al. (2019b), we derived the central frequency and polarization sense of the observed EMIC waves every 1 min during the wave event interval.

Figure 1 presents an EMIC wave event observed by the Arase satellite on January 4th 2019 at 1500-1620 UT: a background electron density derived from the UHR frequency (Figure 1a), the dynamic spectrum of the perpendicular component of the magnetic field with the equatorial gyro frequencies for H^+, He^+, and O^+ (Figure 1b), temperature anisotropy $T_\perp/T_\parallel$ (Figure 1c), parallel plasma beta $\beta_\parallel$ (Figure 1d), and proton pitch-angle distributions at different energy ranges (Figure 1f-1k). EMIC waves were well-defined below f_{cHe}, as He-EMIC waves, at 1520-1600 UT (Figure 1b). The Arase satellite was located ~18 MLT at L~6 near the magnetic equator (MLAT~5˚), with a background density of 80 cm^{-3} (Figure 1a). $T_\perp/T_\parallel$ suddenly dropped and quickly recovered to its initial value immediately before onset of the EMIC wave (~1520 UT) (Figure 1c). Figure 1d shows an increase in $\beta_\parallel$ just before the EMIC wave event, which remained roughly constant during the event. The proton omniflux distributions revealed flux enhancement at energies from 100 keV/q with the EMIC wave event, the lower boundary of which extended to several keV/q (Figure 1e). Note that the $E_{p,min}$ at 1540-1545 UT was discontinuous as the central frequency was not selected due to out of our event criteria between the two EMIC wave portions.

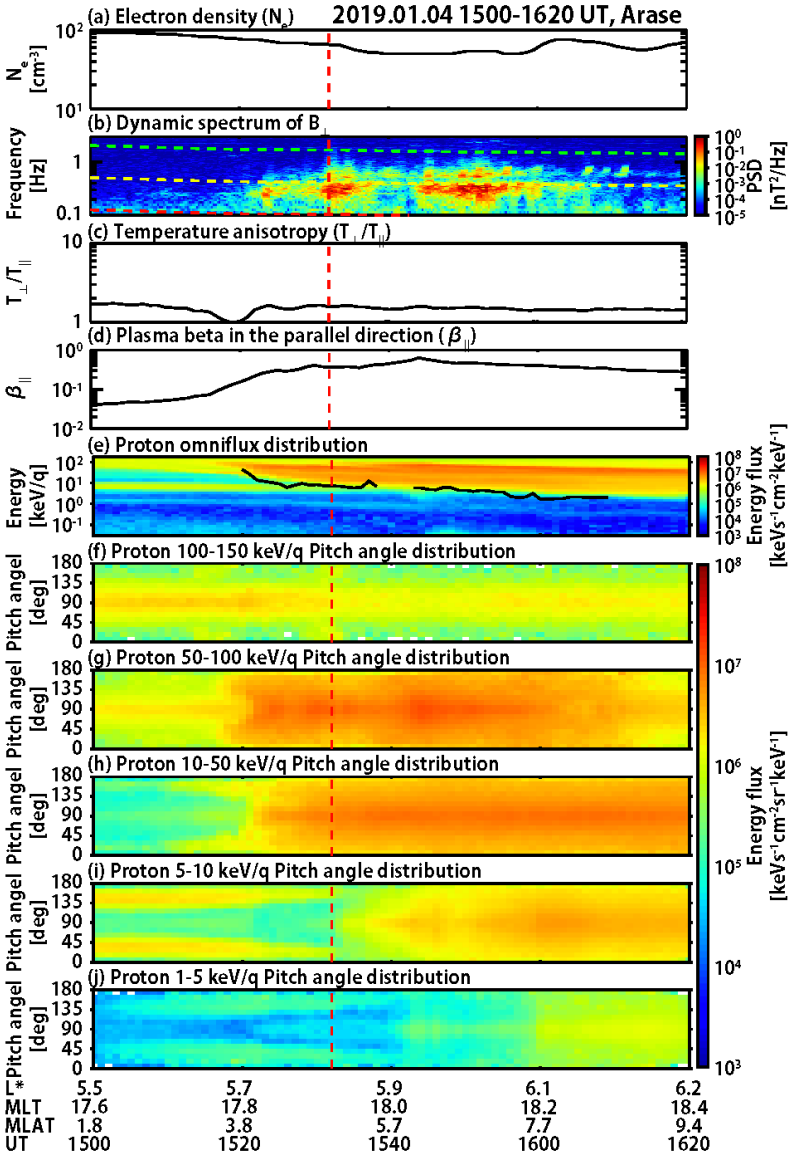

Figure 1. An EMIC wave event on January 4th, 2019 at 1500-1620 UT observed by the Arase satellite. (a) Background electron density (N_e), (b) perpendicular dynamic spectrum of the magnetic field ($B_\perp$) obtained by the MGF instrument, (c) temperature anisotropy ($T_\perp/T_\parallel$), (d) parallel plasma beta ($\beta_\parallel$), (e) energy spectrum of inter-calibrated proton omniflux distribution, and (f-k) pitch-angle distributions of energetic protons at energies of (f) 100-150, (g) 50-100, (h) 10-50, (i) 5-10, (j) 1-5 keV/q. The green, yellow, and red curves in Figure 1b represent the equatorial H^+, He^+, and O^+ gyrofrequencies, respectively. The red horizontal dashed line indicates 1532-1533 UT shown in Figure 2. The black solid curve in Figure 1e denotes the computed minimum proton resonance energy ($E_{p,min}$) using the central frequencies of observed He-EMIC waves.

We focused on the development of energetic proton distributions associated with EMIC waves. The variation of $E_{p,min}$ gradually decreased from 44.2 to 1.8 keV (Figure 1e) and was well consistent with the lower boundary of the H^+ flux enhancements. This indicates that the proton

flux enhancement in this energy range may be related to the major drivers of the observed EMIC waves. Figures 1g-1j present the proton pitch angle distributions at different energy steps. Except for the 100-150 keV/q range (Figure 1f), energy fluxes at energies of 1-100 keV/q (Figures 1g-1k) generally exhibited sudden enhancement among all pitch angles during the EMIC wave event, and the highest energy fluxes appeared at pitch angle of 90˚. Interestingly, Figures 1h-1j show that the pitch angle structures seemed to be immediately shifted from field-aligned to pancake-like distributions when $E_{p,min}$ reached the energy ranges of the lower boundary of the sudden flux enhancement. This sudden change in energetic proton distributions depending on $E_{p,min}$ probably occurred from the mixture of not only the energetic particle input driving EMIC waves, but also the pancake distributions by EMIC pitch-angle scattering.

We described $E_{p,min}$ by solving the cold plasma dispersion relation based on the parameters observed during wave activity. Figure 2 shows an example of the dispersion relation (Figure 2a) and the corresponding $E_{p,min}$ (Figure 2b) at the time marked by the red dashed line in Figure 1. The parameters used for these calculations are labeled in Figure 2. First, we obtained $k_{\parallel}$ from the dispersion relation (Figure 2a) using the central frequency with the peak wave power. We then applied $v_{\parallel}$ obtained from Eq. (5) to finalize $E_{p,min}$ (Figure 2b). In Figure 2, the central frequency was 0.3 Hz (a normalized frequency of 0.18 f_{cH}); thus the corresponding $E_{p,min}$ was 7.22 keV. $E_{p,min}$ was recorded every 1 min during the wave duration(black solid line in Figure 1e).

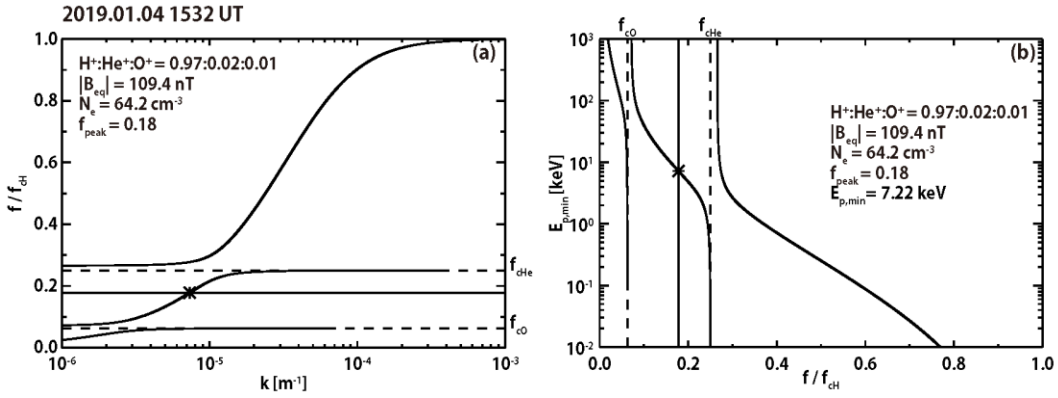

Figure 2. (a) Dispersion relation and (b) corresponding minimum resonance energy at 1532-1533 UT on January 4th, 2019. The parameters used for this calculation are indicated in the figure.

3 Statistical Results

From the event selection, we identified 211.4 and 517.5 hrs of H- and He-EMIC waves, respectively, observed by the Arase satellite from May 2017 to December 2020.

3.1 Spatial Distributions of EMIC waves and Electron Density

We identified EMIC waves for a 43-month period (May 2017-December 2020) using Arase observations. Figure 3 presents the distributions of dwell times and EMIC wave occurrence rates in the L*-MLT plane. The bin sizes for L*-MLT were 1 h in MLT with 0.5 in L* shell in the L* range in 2-9. The dwell time of the Arase satellite was well distributed over all MLT and L* shells, providing sufficient spatial coverage to investigate the statistical characteristics of EMIC waves in the inner magnetosphere (Figure 3a). Occurrence rates of the EMIC waves were evaluated as the total observed EMIC wave time divided by the dwell time in each bin (Figure 3b). We took into account only the regions where the wave occurrence rate exceeded 1 % to focus on the major EMIC wave generation regions. Two significant peak EMIC wave distributions were observed: 3-8 MLT at L* = 7.5-9 and 11-20 MLT at L* = 5-9. These distributions were consistent with the results of previous studies using in-situ satellite observations (e.g., Jun et al., 2021; Keika et al., 2013; Min et al. 2012; Usanova et al., 2016).

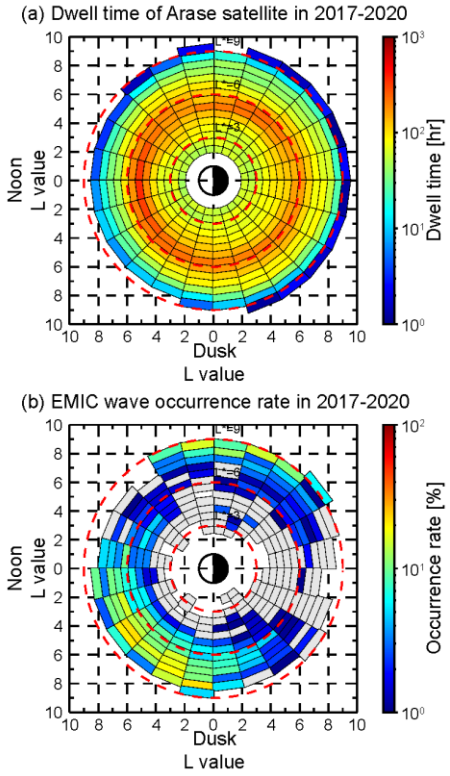

Figure 3. (a) Dwell time and (b) EMIC wave distribution in the L*-MLT plane observed by the Arase satellite from May 2017 to December 2020. The gray regions indicate EMIC wave occurrence rate < 1 %. The red circles denote L* = 3,6, and 9.

Figure 4 presents the MLAT distributions of dwell times and EMIC wave occurrence rates for each 6-hour MLT bin. The bin sizes for Re-MLAT were 0.5 in Re with 5˚ in MLAT in the MLAT range of |40|˚. Even though the Arase satellite had limited observations in the Southern Hemisphere at 09-15 MLT bin due to its orbit in 2017-2020, we had sufficient observational coverage for this study (Figures 4a-4d). We found that EMIC waves were predominant at higher MLAT (Figures 4e-4h). Typical EMIC waves were generated near the magnetic equator and

propagated to higher latitudes along the field line. Previous studies (Usanova et al., 2012; Min et al., 2012) have reported higher EMIC wave occurrence rates in the outer magnetosphere. Therefore, the appearance of peak EMIC wave occurrence at higher MLAT resulted from the propagated waves at higher L* shells. It should be noted that the MLAT distributions of EMIC waves with broad observational coverage in this study were facilitated by novel high-MLAT measurements made by the Arase satellite.

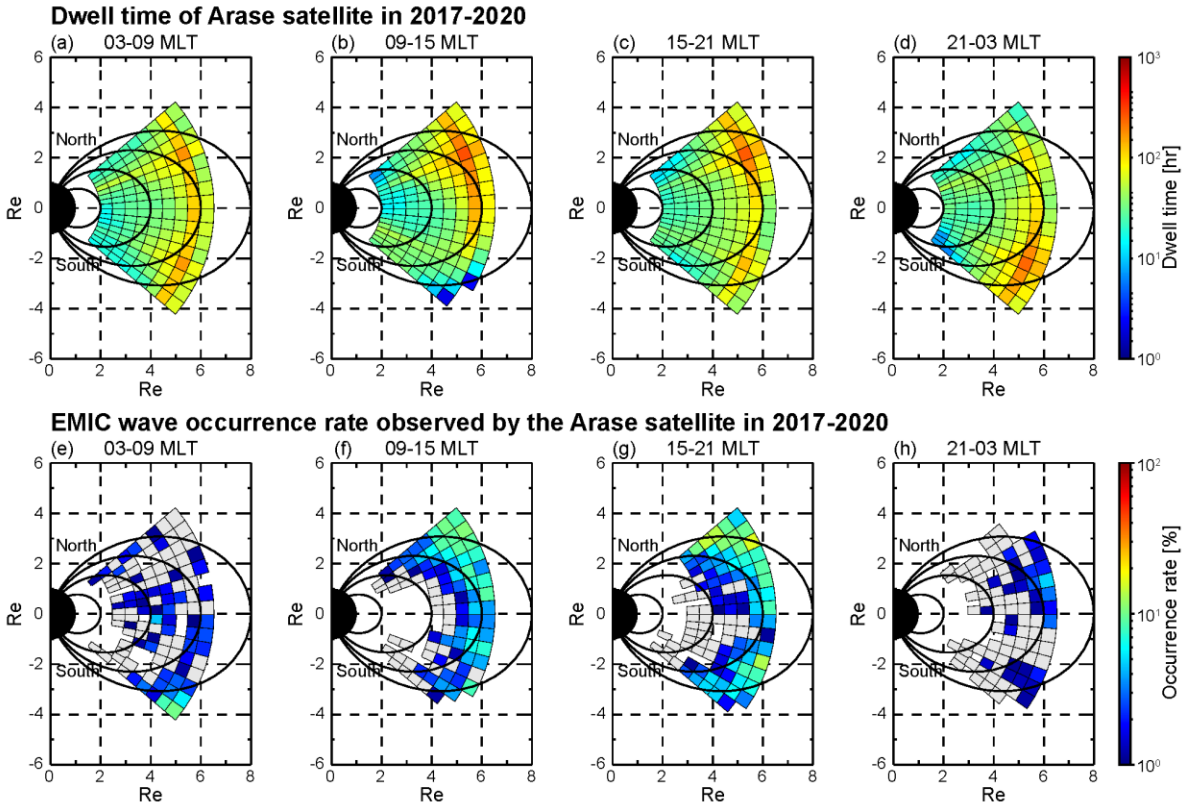

Figure 4. (a-d) Dwell time and (e-h) EMIC wave distribution at each 6-hour MLT sector in the Re-MLAT plane observed by the Arase satellite from May 2017 to December 2020. The gray regions indicate EMIC wave occurrence rate < 1 %. The black curves show the field lines at L*=2,4,6, and 8.

In Figure 5, all EMIC wave events were divided into H- and He-EMIC waves according to equatorial ion gyrofrequencies using the estimated equatorial magnetic field intensity from the TS05 geomagnetic model. To investigate the dependence on background electron density, we averaged the electron densities associated with EMIC waves in each bin.

Based on Figure 5, we identified three distinct wave occurrence regions with the wave occurrence rate > 10 %, depending on the frequency band and N_e. In Figure 5a, H-EMIC waves had two different peak occurrence regions in 3-8 MLT at L* = 7.5-9 (Peak Region 1; PR1) and in 12-15 MLT in L*=6.5-8 (Peak Region 2; PR2). Both regions exhibited lower N_e (< 10 cm^{-3}) as seen in Figure 5c, indicating that the waves were observed outside the plasmasphere. However, He-EMIC waves showed a broad occurrence region at 12-20 MLT at L* = 5.5-85 (Peak Region 3;

PR3) in Figure 5b. As N_e in the broad occurrence region gradually decreased from lower to higher L* shells as shown in Figure 5d, it is difficult to simply identify whether wave activities occurred inside or outside the plasmasphere. If we adopt a specific value of $N_e \sim 40 cm^{-3}$ (e.g., Goldstein et al., 2014) as a proxy to roughly locate the plasmapause, we can assume that He-EMIC waves in PR3 occurred either inside the plasmasphere, plasmaspheric plumes, or near the plasmapause. The dawn-dusk asymmetry of the peak occurrence regions between H- and He-EMIC waves agreed well with the EMIC wave distributions obtained by previous in-situ satellite observations (e.g., Min et al., 2012; Kim et al., 2016b; Jun et al., 2021).

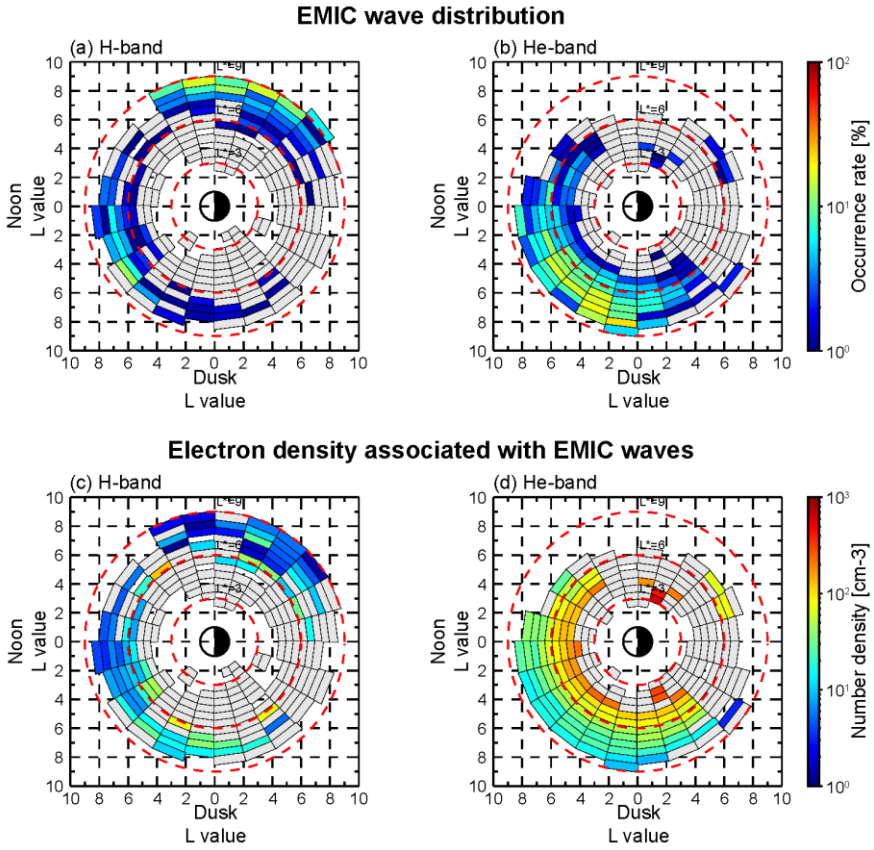

Figure 5. (a) H- and (b) He- EMIC occurrence rates, and related electron density distributions for (c) H-band and (d) He-band.

3.2 Temperature Anisotropy-Parallel Plasma Beta conditions with EMIC waves

Even though the temperature anisotropy $T_\perp/T_\parallel$ and parallel plasma beta $\beta_\parallel$ varied with the EMIC wave activity (Figure 1), it was not sufficient to demonstrate the relationship between these parameters and EMIC wave activity from a single case study. Thus, we examined their inverse relationship between $T_\perp/T_\parallel$ and $\beta_\parallel$ associated with EMIC waves through a statistical analysis (Figure 6) showing the statistical results of EMIC wave distributions (Figures 6a-6b), |MLAT| (Figures 6c-6d), and polarization sense (Figures 6e-6f) in $T_\perp/T_\parallel$- $\beta_\parallel$ diagrams for H- and He-EMIC waves. The threshold of proton cyclotron instability is defined by Eq. (1) (Blum et al 2009; Denton

et al., 1994; Gary et al., 1994; Yue et al., 2019). We obtained a=1.3 and b=0.35 by the upper fitting boundary of our observations, and the threshold lines were marked with the black dashed curves in Figure 6.

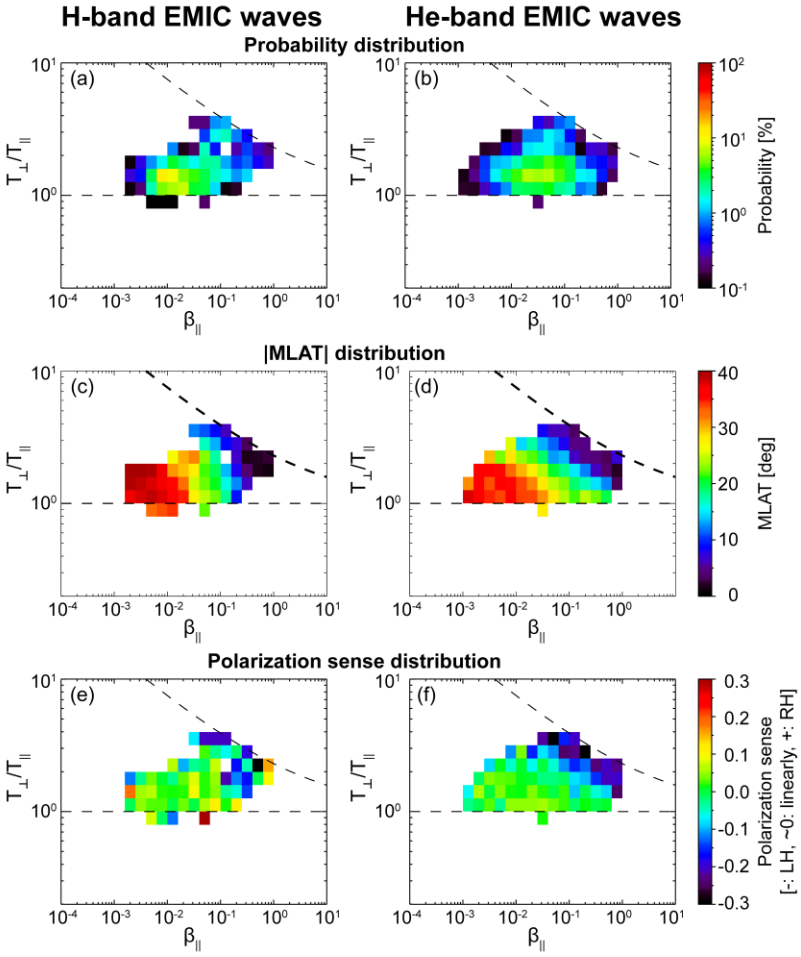

Figure 6. Distribution of (a-b) probability of EMIC waves, (c-d) average |MLAT|, (e-f) polarization sense for H- and He-EMIC waves as a function of proton temperature anisotropy and parallel plasma beta based on the Arase observations from May 2017 to December 2020. The dashed curve on each panel is the threshold of proton cyclotron instability obtained from plasma kinetic theory of $\frac{T_\perp}{T_\parallel} = 1 + \frac{a}{\beta_\parallel^b}$. We used a=1.3 and b= 0.35 obtained by the upper profile of EMIC wave distributions.

Overall, EMIC waves exhibited significant tendencies in |MLAT| and polarization sense depending on the plasma conditions regardless of the wavebands. The observed EMIC waves near the threshold of the proton cyclotron instability had left-handed polarization close to the magnetic equator (< 5˚ |MLAT|), indicating that they were generated near the magnetic equator. As |MLAT| increased, the polarization sense for He-EMIC waves clearly varied from left-handed to linear polarization (Figures 6d and 6f), while the polarization sense for H-EMIC waves appeared roughly constant with linearly polarization even near the magnetic equator (Figures 6c and 6e). The former

indicates polarization reversal during propagation from the wave source region to higher latitudes due to the changing magnetic field intensity (Kim et al., 2016a). We also found that the latitude of the changing polarization sense from left-handed to linear was ~ 20˚ MLAT (Figure 5g), corresponding to the crossover latitudes of EMIC waves in previous studies (e.g., Loto'aniu et al., 2005; Jun et al., 2019b; Yue et al., 2019). The latter is related to linearly polarized H-EMIC waves by the solar wind dynamic pressure variations as reported by Jun et al. (2019b).

3.3 Proton Distributions associated with EMIC waves

To investigate the influence of EMIC waves on energetic proton distributions in each region, the energetic proton PAD associated with EMIC waves (top panels) and the energy flux ratio of the PAD between with and without EMIC waves (bottom panels) were presented (Figure 7). The PAD was binned with a bin size of 11.25˚ for the pitch angle and energy range from 30 eV to 185 keV at each peak occurrence region. Figures 7a-7c show the average PAD associated with EMIC waves in each peak occurrence region. Figures 7d-7f show the flux ratio between cases with and without EMIC waves in each peak occurrence region. The reddish and bluish regions indicate an increase and decrease in the proton flux associated with EMIC waves, respectively. We assumed that an increase in proton flux with EMIC waves at all pitch angles at certain energies is strongly related to not only energetic particle input as the free energy source of EMIC waves, but also the deformation of pitch-angle scattering by EMIC wave-particle interaction (e.g., Sigsbee et al., 2019).

Proton distributions associated with EMIC waves differed significantly depending on peak occurrence regions (Figure 7), supporting that EMIC waves supports that EMIC waves have different free energy sources depending on their geomagnetic environments (Jun et al., 2021).

For example, Figure 7a shows the weakest flux level among the three regions. Instead, PR1 shows a clear flux enhancement in the warm plasma energy range (E < 10 keV/q) over the entire pitch-angle range compared to the other regions (Figures 7a nad 7d). This is related to the supply of warm protons (E < 10 keV) due to $\mathbf{E} \times \mathbf{B}$ drift by the combination of the electric and magnetic fields (Yue et al., 2018). For PR2 (Figures 7b and 7e), we observed two types of flux enhancements associated with EMIC waves. One appeared at energies of 1-100 keV/q in field-aligned directions, and the other was among all pitch-angles over a limited energy range of 2-8 keV/q. Figure 7c for PR3 that shows the highest flux level appeared at energies of 1-100 keV/q among all the peak occurrence regions. We also found a significant increase in the proton energy flux > 2 keV/q at all pitch-angles for PR3 (Figure 7f). This hot proton population is transported from the plasma sheet in the magnetotail to the dusk sector during the substorm intervals, and contributes to drive the temperature anisotropy, causing enhanced EMIC waves in the afternoon sector (e.g., Saikin et al., 2016; Jun et al., 2019a and 2021). PR3 showed the another flux enhancement in the warm plasma region (E < 100 eV) which might be due to another processes such as EMIC wave heating by non-linear wave-particle interactions (Ma et al., 2019; Shoji et al.,2021).

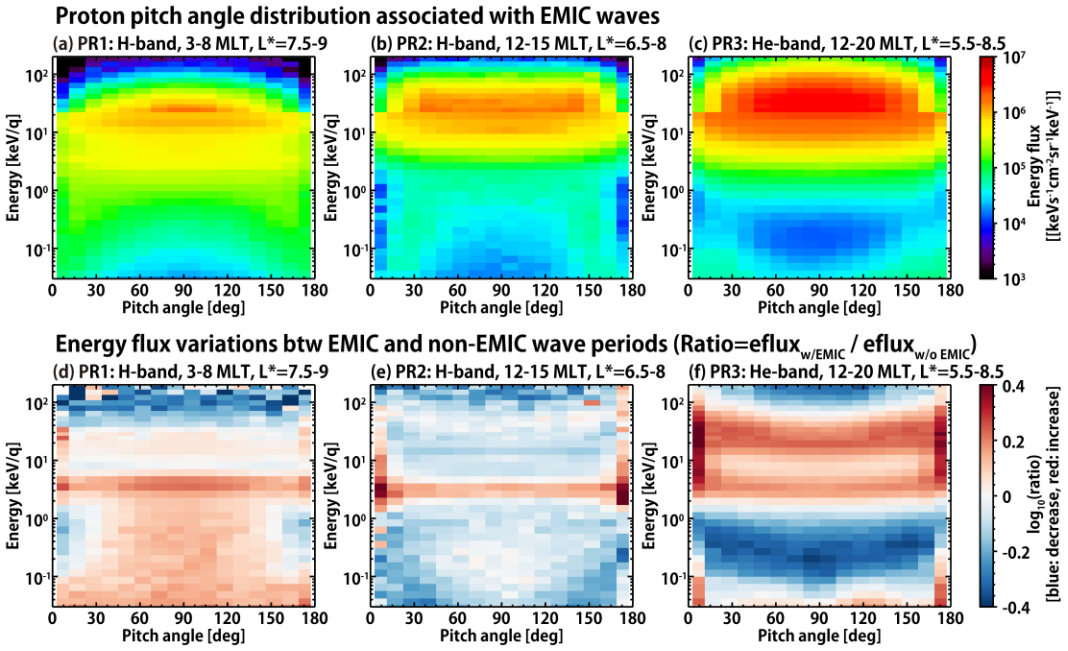

Figure 7. (a-c) Proton pitch-angle distribution associated with EMIC waves as a function of energy and pitch angle at each peak occurrence region. (d-f) Energy flux ratio between with and without EMIC waves at each peak occurrence region.

3.4 The Relationship Between EMIC Wave Frequency and Minimum Resonance Energy

Figure 8 shows the normalized distributions of $E_{p,min}$ as a function of the frequency normalized by f_{cH} in each peak occurrence region. We took the central frequency that satisfied our event selection criteria for the calculation of $E_{p,min}$ during the EMIC wave periods. The vertical dashed lines denote ion gyrofrequencies (f_{cH}, f_{cHe}, and f_{cO}). The bin sizes of the normalized frequency and $E_{p,min}$ were 0.01 on a linear scale and 0.05 on a logarithic scale, respectively. We adopted two ion compositions for two different wavebands: H^+:He^+:O^+=0.85:0.1:0.05 for H-EMIC waves (PR1 and PR2), and H^+:He^+:O^+=0.97:0.02:0.01 for He-EMIC waves (PR3) (Section 2.4). The vertical closed arrow bars in each panel indicate the observed energy ranges, showing an increase in proton fluxes obtained from Figure 7d-7f. We divided the total number of data points in each peak occurrence region to obtain the normalized distributions.

Overall, the $E_{p,min}$ distributions in all regions were in good agreement with the energy range where the flux enhancements were associated with the EMIC waves (Figures 7d-7f). We also found distinct distributions at each peak occurrence region. Even though PR1 and PR2 took into account same waveband (H-EMIC waves), the $E_{p,min}$distributions were completely different. Because the normalized frequency for PR1 was widely distributed from 0.3 to 0.9, $E_{p,min}$ varied from 1 eV to 100 keV with a uniform distribution (Figure 8a). $E_{p,min}$ was locally distributed from 1 keV to 1 MeV, with limited normalized frequencies of 0.3-0.5 (Figure 8b). For PR3 (Figure 8c), the observed energy ranges with flux enhancements were consistent with the peak $E_{p,min}$

492 distributions located at 2-100 keV, except for the region at energies of < 100 eV.

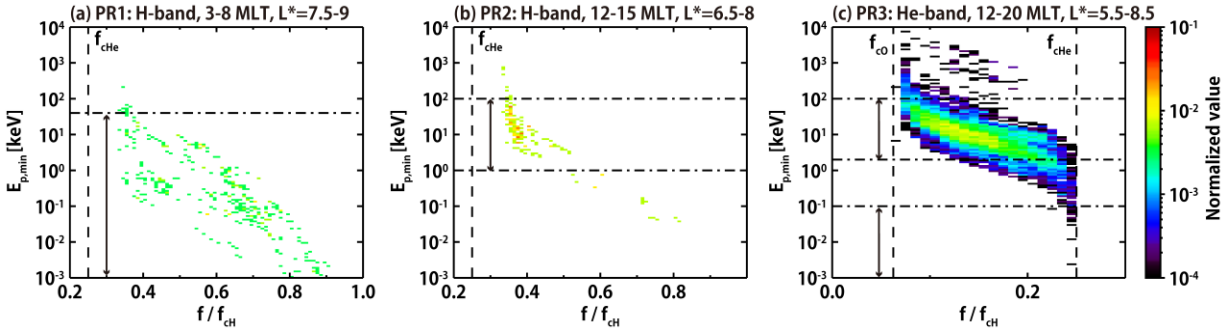

493

494 **Figure 8.** Normalized distribution as a function of the proton minimum resonance energy
495 ($\boldsymbol{E_{p,min}}$) and normalized frequency by f_{cH} for each peak occurrence region. Vertical dashed lines
496 represent the equatorial ion gyrofrequencies. Horizontal dashed lines denote the observed flux
497 enhancement energy range obtained from Figure 7.

498

499 **4 Discussion**

500 In this study, we investigated the spatial distributions of EMIC waves and their associated
501 energetic proton distributions in the inner magnetosphere using the Arase satellite data from May
502 2017 to December 2020. We found three distinct peak occurrence regions of EMIC waves
503 depending on the waveband and the related background electron density. The observational and
504 theoretical characteristics of EMIC waves within each peak occurrence region are summarized in
505 Table 1.

	Peak Region 1 (PR1)	Peak Region 2 (PR2)	Peak Region 3 (PR3)
Peak occurrence regions	03-08 MLT, L* = 7.5-9	12-15 MLT, L* = 6.5-8	12-20 MLT, L* = 5.5-7.5
Waveband	H-band	H-band	He-band
Electron density	N_e < 10 cm^{-3} (outside the plasmasphere)	N_e ~ 10-20 cm^{-3} (outside the plasmasphere)	N_e ~ 50-100 cm^{-3} (inside or near the plasmasphere)
Proton distributions associated	Weakest flux level among all regions.	Similar distributions with PR1.	Strongest ring current population at E = 1-187 keV

with EMIC waves	Flux enhancements: - E < 40 keV/q (warm proton populations)	Flux enhancements: -E = 1-100 keV/q (field-aligned directions) -E = 2-4 keV/q (all pitch-angles)	Flux enhancements: -E = 2-187 keV/q -E < 100 eV/q (field-aligned directions)
The computed minimum resonance energy ($\boldsymbol{E_{p,min}}$)	1 eV - 100 keV	1 keV - 1 MeV (some portions at ~0.1 keV)	0.1 keV - 1 MeV

Table 1. Summary of the characteristics of EMIC waves at four distinct peak occurrence regions observed by the Arase satellite.

4. 1. The relationship between plasma kinetic theory and EMIC waves

We examined the inverse relationship between $T_{\perp,p}/T_{\parallel,p}$ and $\beta_{\parallel,p}$ associated with EMIC waves as shown in Figure 6. EMIC waves were observed only in the anisotropy range between the threshold of the proton cyclotron instability and $T_{\perp,p}/T_{\parallel,p}$ >1. In particular, the highest probability of EMIC waves with left-handed polarization at the magnetic equator was near the threshold of the proton cyclotron instability. After EMIC wave generation within the source regions, they propagate approximately along the field lines to higher magnetic latitudes and experience a change in the dispersion relation (Matsuda et al., 2021). We found that the polarization sense varied from left-handed to linear as |MLAT| increased, indicating mode coupling and conversion during the propagation of EMIC waves. Because the polarization sense changed to linear at |MLAT| ~ 20˚ on average, this result was consistent with previous statistical studies of the EMIC wave source boundaries on MLAT (e.g., Loto'aniu et al., 2005; Jun et al., 2019b; Yue et al., 2019). The probability distribution of EMIC waves in $T_{\perp,p}/T_{\parallel,p}$-$\beta_{\parallel,p}$ diagram shifted away from the threshold of proton cyclotron instability to a lower $\beta_{\parallel,p}$ with a constant $T_{\perp,p}/T_{\parallel,p}$with an increase in |MLAT|. This result can be explained by the average meridional distribution of hot (10-180 keV) protons as shown by the Arase satellite (Imajo et al., 2019). Pressure anisotropy is roughly constant with increasing MLAT, whereas $\beta_{\parallel,p}$ decreases as MLAT increases.

If $T_{\perp,p}/T_{\parallel,p}$ is independent and roughly constant on |MLAT|, we can assume an equatorial parallel plasma beta using the estimated magnetic field intensity at the magnetic equator obtained by the TS05 model. Figure 9 shows the probability distributions of EMIC waves in $T_{\perp,p}/T_{\parallel,p}$-$\beta_{\parallel,p}$ diagram within each peak region. The upper and lower panels use the local and equatorial magnetic field intensities, respectively. Although we cannot estimate the appropriate $P_{\parallel,p}$ at the magnetic

equator, the highest probability of EMIC waves obtained from the equatorial parallel plasma beta shifted near the threshold of ion cyclotron instability, except for PR2 (Figures 9d-9f).

If the threshold of ion cyclotron instability and the equatorial plasma parameters are well-determined from observational and theoretical methods, we suggest that the inverse relationship between $T_{\perp,p}/T_{\parallel,p}$ and $\beta_{\parallel,p}$ can be used as a proxy for the generation conditions of EMIC waves using local plasma conditions. When the plasma condition is unstable for proton cyclotron instability due to sufficient temperature anisotropy, EMIC waves are generated. During this process, plasma distribution undergoes diffusion in the velocity space by EMIC wave-particle interaction, leading to isotropic distributions by the ion cyclotron instability to a linear marginally stable state (Denton et al., 2019; Yue et al., 2019). Unfortunately, this approximation for PR2 did not reach the threshold for proton cyclotron instability. Thus, we could not demonstrate a clear interpretation at this point, but we proposed that a non-linear process driven through the formation of proton-hill/hole (Shoji et al, 2018, 2021) might put the distribution far from the stable state. Nakamura et al. (2016) reported that EMIC rising/falling tone emissions caused by a proton-hill/hole distributions were dominantly observed on the dayside at higher magnetic latitudes, consisting of PR2. Future research target should investigate the influence of non-linear effects on EMIC waves.

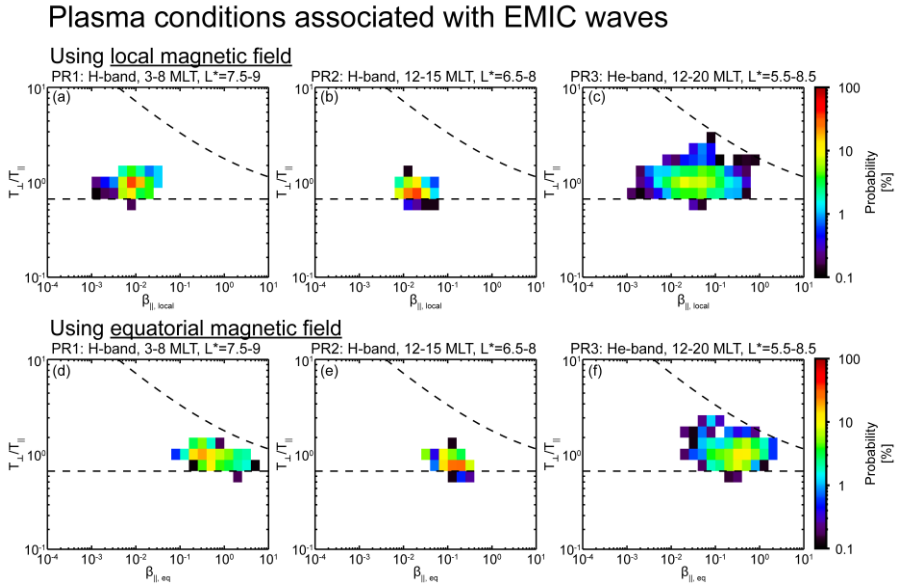

Figure 9. Probability distribution of EMIC waves for each peak occurrence region as a function of proton temperature anisotropy and parallel plasma beta using (a-d) local magnetic field and (e-h) the estimated equatorial magnetic field computed by a TS05 model. The dashed curves on each panel are the thresholds of proton cyclotron instability as same as Figure 6.

4. 2. Possible generation processes and free energy sources of EMIC waves under different geomagnetic environments

In this study, we found that EMIC waves at PR1 occurred in the morning sector at higher

L-shells (L* = 7.5-9) with broadly scattered normalized frequencies of 0.3-0.9. In Figure 7a, the proton distributions associated with EMIC waves at PR1 exhibited the abundant warm proton distributions with weaker ring current populations. The unusual high-frequency EMIC waves near f_{cH} were predominantly observed within this region, and the computed $E_{p,min}$ was distributed broadly from 40 keV to even a few eV. PR1 appeared to have different environments for the generation of EMIC waves compared to those for typical EMIC waves, indicating that the ring current populations having from a few tens to several hundreds of keV, known as typical free energy sources of EMIC waves, are not always sufficient to be the major contributor on the wave generation in the morning sector at higher L shells.

To understand the generation processes of EMIC waves at PR1, we proposed two possibilities: broad source regions and a wide energy range of the free energy sources. If the initial frequencies of EMIC waves are defined by the magnetic field intensity at their source regions, we can assume broader distributions of the normalized frequencies as a result of the radially extended source regions. However, the first assumption did not coincide with our observations (Figure 5a). In contrast, for PR1, flux enhancements associated with EMIC waves appeared with wide energy ranges of < 10 keV/q. Thus, the second possibility was deemed more reliable for EMIC waves at PR1. Previous studies have proposed that the warm plasma cloak (E < 1 keV) with temperature anisotropy in the morning sector can be a potential to drive temperature anisotropy for the EMIC wave generation (Keika et al., 2013; Kim et al., 2016b). The low-energy protons (E < 10 keV) drift to the east (dawn) due to convection and corotation drift motion, while the westward (toward dusk) gradient and curvature drift motions dominate for energetic protons in the energy range of > 10 keV (Yue et al., 2017a, 2017b, and 2018). Using the Van Allen Probes and Arase observations, Jun et al. (2021) reported that morning-side EMIC waves in the H-band were mainly observed under quiet geomagnetic conditions. According to the relationship between the orientation of interplanetary magnetic field (IMF) Bz and EMIC wave distributions (Park et al., 2017), H-EMIC waves have peak occurrence regions in the dawn sector under northward IMF Bz conditions. They suggested that $T_{\perp,p}/T_{\parallel,p}$ in the dawn sector increases due to the dominant effects of E × B drift motion at energies of 1-25 keV during the northward IMF Bz intervals, causing H-EMIC waves in that region.

Moreover, Teng et al. (2019) reported unusual EMIC waves near the proton gyrofrequency associated with enhanced suprathermal protons (10-100 eV). These waves exhibited a very narrow bandwidth and tended to be observed simultaneously with the magnetosonic waves. They also reported that these waves were usually observed in the morning to noon sector based on the Van Allen Probes observations. Asamura et al. (2021) used the Arase observations and identified that magnetosonic waves cause resonant heating of suprathermal protons, which have temperature anisotropy and drive high-frequency EMIC waves in the noon sector. Therefore, we suggest that low-energy proton distribution, such as warm plasma (E < 1 keV), can be a possible candidate as a free energy source for unusual high-frequency H-EMIC waves in the morning sector at higher L-shells during quiet geomagnetic conditions.

We also found the other peak occurrence regions for H-EMIC waves in the noon sector at L* = 6.5-8 (PR2). We could not find a significant coupling of EMIC waves with energetic proton distributions for PR2 in this study. However, the peak EMIC wave occurrence region for R2 was consistent with previous studies of H-EMIC driven in the lower density regions on the dayside by the solar wind dynamic pressure (e.g., Jun et al., 2019a and 2021; Saikin et al., 2013; Park et al.,

2016; Usanova et al., 2012). When the ambient magnetic field is compressed by strong solar wind dynamic pressure, adiabatic heating occurs on the dayside magnetosphere, contributing to the enhancement of temperature anisotropy (Zhou and Tsurutani, 1999). During this process, the temperature anisotropy of energetic protons increases in all energy ranges, exciting EMIC waves on the dayside (Anderson and Hamilton, 1993).

We found a wide spatial distribution of He-EMIC waves from noon to the afternoon sector at L* = 5.5-8.5 with higher background electron densities (PR3). For the He-EMIC waves, the energy range of the obtained $E_{p,min}$ and their associated flux enhancements were in good agreement at 1-180 keV (Figures 7f and 8c). In particular, we found a clear ring current population in the proton PAD and the significant proton flux enhancement occurred in the energy range of 2-100 keV. Based on the Van Allen Probes observations, Jun et al. (2019a) reported that He-EMIC waves associated with particle injections generally occurred inside the plasmasphere in the afternoon sector. Yue et al. (2019) also reported that enhanced He-EMIC waves inside the plasmasphere were predominantly observed near the threshold of the proton cyclotron instability during strong AE intervals. From the current and previous studies, we suggest that the free energy source of EMIC waves for PR3 is the energetic particles transported from the plasma sheet into the inner magnetosphere during disturbed geomagnetic conditions. Hot anisotropic ions in the ring current population play an important role in driving the growth rate of EMIC waves, and the maximum wave growth rate was observed at lower frequencies as He-EMIC waves by the large plasma density (e.g., Cornwall et al., 1970; Lee et al., 2017; Chen et al., 2010). These He-EMIC waves in the afternoon sector are quite effective at resonating with the ring current populations in the cold plasma dominant regions (Jordanova et al., 2008). They also diffuse the hot protons from 90˚ to 0˚ and 180˚ pitch angles, causing the IPAs due to precipitating energetic protons (Sakagushi et al., 2007; Ozaki et al., 2016, 2020) and relativistic electrons (Miyoshi et al., 2008). Unfortunately, we could not interpret the clear reason for the flux enhancements associated with He-EMIC waves at energies < 0.1 keV for PR3 (Figure 7f). We infer a candidate that this might be related to ion heating at lower energies by EMIC wave-particle interactions and magnetosonic waves (Ma et al., 2019; Shoji et al., 2021).

PR3 showed a broad spatial distribution radially with relatively lower densities (Ne~ a few tens cm^{-3}) in the dusk sector at L* = 7-9 at higher |MLAT| (Figures 4 and 5). This region might have different plasma conditions for the generation of EMIC waves compared to those near the plasmapause, therefore we could not exclude other possibilities, such as off-equatorial generation process as a possible cause of EMIC waves in the dusk sector at higher L-shell regions (e.g., Allen et al., 2015, 2016; Vines et al., 2019). Based on the Arase and the Van Allen Probe observations (Jun et al., 2021), He-EMIC waves outside the plasmasphere were predominantly observed in the dusk sector at higher L-shell regions under moderate geomagnetic conditions. We could not determine whether the observed EMIC waves were freshly generated close to the off-equatorial source regions at higher magnetic latitudes or if they just propagated from the magnetic equator. Such a study can be conducted by examining the Poynting flux of EMIC waves using the magnetic and electric field instruments onboard the Arase satellite, which can be a future approach.

5 Conclusions

In this study, we investigated the spatial distributions of EMIC waves and the energetic

proton distributions associated with them in the inner magnetosphere using the Arase satellite data from May 2017 to December 2020. We found that EMIC waves were generated near the threshold of the proton cyclotron instability at the magnetic equator with a left-handed polarization sense, and propagated to a higher MLAT along the field line. During propagation, EMIC waves suffered polarization reversal at |MLAT|~20˚ from left-handed to linear. If it is possible to estimate the plasma conditions derived by $T_{\perp,p}/T_{\parallel,p}$ and $\beta_{\parallel,p}$ near the magnetic equator and determine an appropriate threshold for the proton cyclotron instability, we can predict the existence of EMIC waves by in-situ observations. We also found three peak occurrence regions of EMIC waves with different characteristics depending on the wavebands and ambient electron densities. We suggest that free energy sources of EMIC waves in different geomagnetic environments drive various types of EMIC waves, and they interact with energetic protons at different energy ranges. We will extend our future research to investigate the resonant conditions of relativistic electrons for different types of EMIC waves using in-situ satellite observations.

Acknowledgments

Arase satellite datasets for this research are available in these in-text data citation references: Kasahara et al. (2018b), Matsuoka et al. (2018b), and Miyoshi et al. (2018c and 2018d) obtained from the ERG Science Center operated by ISAS/JAXA and ISEE/Nagoya University (https://ergsc.isee.nagoya-u.ac.jp/index.shtml.en, Miyoshi et al., 2018b). Science data of the ERG (Arase) satellite in the present study analyzed MGF-L2 64 Hz v03.04, HFA-L2 v01.01, HFA-L3 v01_01, LEPi-L2 v03_00, MEPi-L2 v01_03 and Orbit L2 v02 and L3 TS04 v01 data. Chao Yue gratefully acknowledges support from research grant National Key R&D Program of China 2020YFE0202100, NSFC Grant Numbers: 41974191, and China National Space Administration project D020303. This study is supported by JSPS KAKENHI (15H05815, 15H05747, 16H06286, 17H00728, 20H01959, 21H04526) and the JSPS Bilateral Open Partnership Joint Research Projects (JPJSBP120192504). SI is supported by the Chubei Itoh Foundation and JSPS Grant-in-Aid for Young Scientists (21K13977). The work of CJ, YM, SI, SN, MS, and TH was done at the ERG-Science center.

References

Allen, R. C. et al. (2015), A statistical study of EMIC waves observed by Cluster: 1. Wave properties. *Journal of Geophysical Research: Space Physics*, 120, 5574-5592. doi:10.1002/2015JA021333

Allen, R. C. et al. (2016), A statistical study of EMIC waves observed by Cluster: 2. Associated plasma conditions. *Journal of Geophysical Research: Space Physics*, 121, 6458-6479. doi:10.1002/2016JA022541

Anderson, B. J., Erlandson, R. E., & Zanetti, L. J. (1992a), A statistical study of Pc1-2 magnetic pulsations in the equatorial magnetosphere: 1. Equatorial occurrence distributions. *Journal of Geophysical Research*, 97(A3), 3075-3088, doi:10.1029/91JA02706

Anderson, B. J., Erlandson, R. E., & Zanetti, L. J. (1992b), A statistical study of Pc1-2 magnetic pulsations in the equatorial magnetosphere: 2. Wave Properties. *Journal of Geophysical Research*, 97(A3), 3089-3101. doi:10.1029/91JA02706

Anderson, B. J., & Hamilton, D. C. (1993), Electromagnetic ion cyclotron waves stimulated by modest magnetospheric compressions. *Journal of Geophysical Research*, 98, 11,369-11,382. doi:10.1029/93JA00605

Asamura, K., Kazama, Y., Yokota, S. et al. (2018), Low-energy particle experiments–ion mass analyzer (LEPi) onboard the ERG (Arase) satellite. *Earth Planets Space*, 70, 70. doi:10.1186/s40623-018-0846-0

Asamura, K., Shoji, M., Miyoshi, Y., Kasahara, Y., Kasaba, Y, et al. (2021), Cross-Energy Couplings from Magnetosonic Waves to Electromagnetic Ion Cyclotron Waves through Cold Ion Heating inside the Plasmasphere. *Physics Review Letter*, 127 (24), 245101(7). doi:10.1103/PhysRevLett.127.245101

Blum, L. W., MacDonald, E. A., Gary, S. P., Thomsen, M. F., & Spence, H. E. (2009), Ion observations from geosynchronous orbit as a proxy for ion cyclotron wave growth during storm times. *Journal of Geophysical Research*, 114, A10214. doi:10.1029/2009JA014396

Borovsky, J. E., Valdivia, J.A (2018), The Earth's Magnetosphere: A Systems Science Overview and Assessment. *Surveys in Geophysics*, 39, 817-859. doi:10.1007/s10712-018-9487-x

Chen, L., Thorne, R. M., Jordanova, V. K., Wang, C.-P., Gkioulidou, M., Lyons, L., & Horne, R. B. (2010), Global simulation of EMIC wave excitation during the 21 April 2001 storm from coupled RCM-RAM-HOTRAY modeling. *Journal of Geophysical Research*, 115, A07209. doi:10.1029/2009JA015075.

Cornwall, J. M., Coroniti, F. V., & Thorne, R. M. (1970), Turbulent loss of ring current protons. *Journal of Geophysical Research*, 75, 4699–4709. doi:10.1029/JA075i025p04699

716 Daglis, I. A., Thorne, R. M., Baumjohann, W., & Orsini, S. (1999), The terrestrial ring current:
717 Origin, formation, and decay. *Reviews of Geophysics*, 37(4), 407–438.
718 doi:10.1029/1999RG900009
719
720 De Michelis, P., Daglis, I. A., & Consolini, G. (1999), An average image of proton plasma pressure
721 and of current systems in the equatorial plane derived from AMPTE/CCE-CHEM measurements.
722 *Journal of Geophysical Research*, 104(A12), 28615–28624. doi:10.1029/1999JA900310
723
724 Denton, R. E., Gary, S. P., Anderson, B. J., Fuselier, S. A., & Hudson, M. K. (1994), Low-
725 frequency magnetic fluctuation spectra in the magnetosheath and plasma depletion layer. *Journal*
726 *of Geophysical Research*, 99(A4), 5893–5901. doi:10.1029/93JA02729
727
728 Ebihara, Y., and Miyoshi, Y. (2011), Dynamic Inner Magnetosphere: A Tutorial and Recent
729 Advances. In: Liu W., Fujimoto M. (eds) The Dynamic Magnetosphere. IAGA Special Sopron
730 Book Series, vol 3. Springer, Dordrecht. doi:10.1007/978-94-007-0501-2_9
731
732 Engebretson, M. J., Peterson, W. K., Posch, J. L., Klatt, M. R., Anderson, et al. (2002),
733 Observations of two types of Pc 1-2 pulsations in the outer dayside magnetosphere. *Journal of*
734 *Geophysical Research*, 107(A12), 1451. doi:10.1029/2001JA000198
735
736 Gary, S. P., & Lee, M. A. (1994), The ion cyclotron anisotropy instability and the inverse
737 correlation between proton anisotropy and proton beta. *Journal of Geophysical Research*, 99,
738 11297–11301. doi:10.1029/94JA00253
739
740 Halford, A. J., Fraser, B. J., & Morley, S. K. (2010), EMIC wave activity during geomagnetic
741 storm and nonstorm periods: CRRES results. *Journal of Geophysical Research*, 115, A12248.
742 doi:10.1029/2010JA015716
743
744 Imajo, S., Nosé, M., Kasahara, S.,Yokota, S., Matsuoka, A., Keika, K.,et al. (2019), Meridional
745 distribution of middle-energy protons and pressure-driven currents in the nightside inner
746 magnetosphere: Arase observations. *Journal of Geophysical Research: Space Physics*, 124,5719–
747 5733. doi:10.1029/2019JA026682
748
749 Imajo, S., Miyoshi, Y., Kazama, Y. et al. (2021), Active auroral arc powered by accelerated
750 electrons from very high altitudes. *Scientific reports*, 11, 1610. doi: 10.1038/s41598-020-79665-5
751
752 Jahn et al., 2017 Jahn, J. M., Goldstein, J., Reeves, G. D., Fernandes, P. A., Skoug, R. M., Larsen,
753 B. A., & Spence, H. E. (2017), The warm plasma composition in the inner magnetosphere during
754 2012–2015. *Journal of Geophysical Research: Space Physics*, 122, 11,018–11,043.
755 doi:10.1002/2017ja024183
756
757 Jordanova, V. K., Albert, J., and Miyoshi, Y. (2008), Relativistic electron precipitation by EMIC
758 waves from self-consistent global simulations, *Journal of Geophysical Research: Space Physics*,
759 113, A00A10. doi:10.1029/2008JA013239
760

Jun, C.-W., Yue, C., Bortnik, J., Lyons, L. R., Nishimura, Y., Kletzing, C., Wygant, J., & Spence, H. (2019a), A statistical study of EMIC waves associated with and without energetic particle injection from the magnetotail. *Journal of Geophysical Research: Space Physics*, 124, 1-18. doi:10.1029/2018JA025886

Jun, C.-W., Yue, C., Bortnik, J., Lyons, L. R., Nishimura, Y. T., & Kletzing, C. A. (2019b), EMIC wave properties associated with and without injections in the inner magnetosphere. *Journal of Geophysical Research: Space Physics*, 124, 2029-2045. doi:10.1029/2018JA026279

Jun, C.-W., Miyoshi, Y., Kurita, S., Yue, C., Bortnik, J., Lyons, L., et al. (2021), The characteristics of EMIC waves in the magnetosphere based on the Van Allen Probes and Arase observations. *Journal of Geophysical Research: Space Physics*, 126, e2020JA029001. doi:10.1029/2020JA029001

Kanekal, S., and Miyoshi, Y. (2021), Dynamics of the terrestrial radiation belts: A review of recent results during the VarSITI (Variability of the Sun and Its Terrestrial Impact) era, 2014-2018. *Progress in Earth and Planetary Science*, 8, 35. doi:10.1186/s40645-021-00413-y

Kasahara, Y., Kasaba, Y., Kojima, H. et al. (2018a), The Plasma Wave Experiment (PWE) on board the Arase (ERG) satellite. *Earth, Planets and Space*, 70, 86. doi:10.1186/s40623-018-0842-4

Kasahara, Y., et al. (2018b), The PWE/HFA instrument Level-2 spectrum data of Exploration of energization and Radiation in Geospace (ERG) Arase satellite. doi:10.34515/DATA.ERG-10000

Keika, K., Takahashi, K., Ukhorskiy, A. Y., & Miyoshi, Y. (2013), Global characteristics of electromagnetic ion cyclotron waves: Occurrence rate and its storm dependence. *Journal of Geophysical Research*, 118, 4,135-4,150. doi:10.1002/jgra.50385

Kim, E.-H., & Johnson, J. R. (2016), Full-wave modeling of EMIC waves near the He^{+} gyrofrequency. *Geophysical Research Letters*, 43, 13-21. doi:10.1002/2015GL066978

Kim, G.-J., Kim, K.-H., Lee, D.-H., Kwon, H.-J., and Park, J.-S. (2016b), Occurrence of EMIC waves and plasmaspheric plasmas derived from THEMIS observations in the outer magnetosphere: Revisit. *Journal of Geophysical Research: Space Physics*, 121, 9,443-9,458. doi:10.1002/2016JA023108

Kozyra, J. U., Cravens, T. E., Nagy, A. F., Fontheim, E. G., and Ong, R. S. B. (1984), Effects of energetic heavy ions on electromagnetic ion cyclotron wave generation in the plasmapause region. *Journal of Geophysical Research: Space Physics*, 89(A4), 2217-2233. doi:10.1029/JA089iA04p02217

Kumamoto, A., Tsuchiya, F., Kasahara, Y., Kasaba, Y., Kojima, H., Yagitani, S., et al. (2018), High frequency analyzer (HFA) of Plasma Wave Experiment (PWE) onboard the Arase spacecraft. *Earth, Planets and Space*, 70, 82. doi: 10.1186/s40623-018-0854-0

807 Kurita, S., Miyoshi, Y., Shiokawa, K., Higashio, N., Mitani, T., et al. (2018), Rapid Loss of
808 Relativistic Electrons by EMIC Waves in the Outer Radiation Belt Observed by Arase, Van Allen
809 Probes, and the PWING Ground Station., *Geophysical Research Letters*, 45, 12720-12729.
810 doi:10.1029/2018GL080262
811
812 Lee, D.-Y., Noh, S.-J., Choi, C.-R., Lee, J. J., & Hwang, J. A. (2017), Effect of hot anisotropic
813 He^+ ions on the growth and damping of electromagnetic ion cyclotron waves in the inner
814 magnetosphere. *Journal of Geophysical Research*, 122, 4,935-4,942. doi:10.1002/2016JA023826
815
816 Li, W., and Hudson, M. K. (2019), Earth's Van Allen radiation belts: From discovery to the Van
817 Allen Probes era. *Journal of Geophysical Research: Space Physics*, 124, 8319-8351. doi:10.1029/
818 2018JA025940
819
820 Lin, R. -L., Zhang, J.-C., Allen, R. C., Kistler, L. M., Mouikis, C. G., Gong, J.-C., et al. (2014),
821 Testing linear theory of EMIC waves in the inner magnetosphere: Cluster observations. *Journal*
822 *of Geophysical Research: Space Physics*, 119, 1004–1027. doi:10.1002/2013JA019541
823
824 Loto'aniu, T. M., Fraser, B. J., & Waters, C. L. (2005), Propagation of electromagnetic ion
825 cyclotron wave energy in the magnetosphere. *Journal of Geophysical Research*, 110, A07214.
826 doi:10.1029/2004JA010816
827
828 Ma, Q., Li, W., Yue, C., Thorne, R. M., Bortnik, J., Kletzing, C. A., et al. (2019), Ion heating by
829 electromagnetic ion cyclotron waves and magnetosonic waves in the Earth's inner magnetosphere.
830 *Geophysical Research Letters*, 46. doi:10.1029/2019GL083513
831
832 Matsuda, S., Kasahara, Y., Miyoshi, Y., Nomura, R., Shoji, M., Matsuoka, A., et al. (2018a),
833 Spatial distribution of fine-structured and unstructured EMIC waves observed by the Arase
834 satellite. *Geophysical Research Letters*, 45, 11,530-11,538. doi:10.1029/2018GL080109
835
836 Matsuda, S., Kasahara, Y., Kojima, H., Kasaba, Y., Yagitani, S., Ozaki, M., et al. (2018b),
837 Onboard software of Plasma Wave Experiment aboard Arase: Instrument management and signal
838 processing of waveform capture/onboard frequency analyzer. *Earth, Planets and Space*, 70, 75.
839 doi:10.1186/s40623-018-0838-0
840
841 Matsuda, S., Miyoshi, Y., Kasahara, Y., Blum, L., Colpitts, C., Asamura, K., et al. (2021).
842 Multipoint measurement of fine-structured EMIC waves by Arase, Van Allen Probe A, and ground
843 stations. *Geophysical Research Letters*, 48, e2021GL096488. doi:10.1029/2021GL096488
844
845 McCollough, J. P., Elkington, S. R., Usanova, M. E., Mann, I. R., Baker, D. N., & Kale, Z. C.
846 (2010), Physical mechanisms of compressional EMIC wave growth. *Journal of Geophysical*
847 *Research*, 115, A10214. doi:10.1029/2010JA015393
848
849 Meredith, N. P., Thorne, R. M., Horne, R. B. , Summers, D., Fraser, B. J., & Anderson, R. R.
850 (2003), Statistical analysis of relativistic electron energies for cyclotron resonance with EMIC
851 waves observed on CRRES. *Journal of Geophysical Research*, 108(A6), 1250.
852 doi:10.1029/2002JA009700

Meredith, N. P., Horne, R. B., Kersten, T., Fraser, B. J., and Grew, R. S. (2014), Global morphology and spectral properties of EMIC waves derived from CRRES observations. *Journal of Geophysical Research: Space Physics*, 119, 5,328-5,342. doi:10.1002/2014JA020064

Min, K., Lee, J., Keika, K., & Li, W. (2012), Global distribution of EMIC waves derived from THEMIS observations. *Journal of Geophysical Research*, 117, A05219. doi:10.1029/2012JA017515

Min, K., Kim, J., Ma, Q. et al. (2021), Unusual high frequency EMIC waves: Detailed analysis of EMIC wave excitation and energy coupling between EMIC and magnetosonic waves. *Advances in Space Research*. doi:10.1016/j.asr.2021.07.039

Miyoshi, Y., Sakaguchi, K., Shiokawa, K., Evans, D., Albert, J., Connors, M., & Jordanova, V. (2008), Precipitation of radiation belt electrons by EMIC waves, observed from ground and space. *Geophysical Research Letters*, 35, L23101. doi:10.1029/2008GL035727\

Miyoshi, Y., Shinohara, I., Takashima, T., Asamura, K., Higashio, N., Mitani, T., et al. (2018a), Geospace exploration project ERG. *Earth, Planets and Space*, 70, 101. doi:10.1186/s40623-018-0862-0

Miyoshi, Y., Hori, T., Shoji, M. et al. (2018b) The ERG Science Center. Earth, Planets, and Space 70, 96. doi:10.1186/s40623-018-0867-8

Miyoshi, Y., Shinohara, I. and Jun, C.-W. (2018c), The Level-2 orbit data of Exploration of energization and Radiation in Geospace (ERG) Arase satellite. doi:10.34515/DATA.ERG-12000

Miyoshi, Y., Shinohara, I. and Jun, C.-W. (2018d), The Level-3 orbit data of Exploration of energization and Radiation in Geospace (ERG) Arase satellite. doi:10.34515/DATA.ERG-12001

Miyoshi, Y., Matsuda, S., Kurita, S.,Nomura, K., Keika, K., Shoji, M., et al. (2019), EMIC waves converted from equatorial noise due to M/Q= 2 ions in the plasmasphere: Observations from Van Allen Probes and Arase. *Geophysical Research Letters*, 46, 5662-5669. doi:10.1029/2019GL083024

Miyoshi, Y., Shinohara, I., Ukhorskiy, S. et al. (2022), Collaborative Research Activities of the Arase and Van Allen Probes, Space Sci Rev, 218, 38. doi:10.1007/s11214-022-00885-4

Nakamura, S., Y. Omura, S. Machida, M. Shoji, M. Nosé, and V. Angelopoulos (2014), Electromagnetic ion cyclotron rising tone emissions observed by THEMIS probes outside the plasmapause. *Journal of Geophysical Research: Space Physics*, 119, 1,874-1,886. doi:10.1002/2013JA019146

Nakamura, S., Omura, Y., and Angelopoulos V. (2016), A statistical study of EMIC rising and falling tone emissions observed by THEMIS. *Journal of Geophysical Research: Space Physics*,121, 8374-8391. doi:10.1002/2016JA022353

Noh, S.-J., Lee, D.-Y., Choi, C.-R., Kim, H., & Skoug, R. (2018), Test of ion cyclotron resonance instability using proton distributions obtained from Van Allen Probe-A observations. *Journal of Geophysical Research: Space Physics*, 123, 6591–6610. doi:10.1029/2018JA025385

Ozaki, M., Shiokawa, K., Miyoshi, Y., Kataoka, R., Connors, M., Inoue, T., et al. (2018), Discovery of 1 Hz range modulation of isolated proton aurora at subauroral latitudes. *Geophysical Research Letters*, 45(3), 1209–1217. doi:10.1002/2017GL076486

Ozaki, M., Shiokawa, K., Horne, R. B., Engebretson, M. J., Lessard, M., Ogawa, Y., et al. (2021), Magnetic conjugacy of Pc1 waves and isolated proton precipitation at subauroral latitudes: Importance of ionosphere as intensity modulation region. *Geophysical Research Letters*, 48, e2020GL091384. doi:10.1029/2020GL091384

Park, J.-S., Kim, K.-H., Shiokawa, K., Lee, D.-H., Lee, E., Kwon, H.-J., Jin, H., & Jee, G. (2016), EMIC waves observed at geosynchronous orbit under quiet geomagnetic conditions (Kp<1). *Journal of Geophysical Research*, 121, 1,377-1,390. doi:10.1002/2015JA021968

Park, J.-S., Shue, J.-H., & Kim, K.-H. (2017), Dependence of electromagnetic ion cyclotron wave occurrence on north-south orientation of interplanetary magnetic field: THEMIS observations. Journal of Geophysical Research: Space Physics, 122, 11,354–11,372. doi:10.1002/2017JA024507

Saikin, A. A., Zhang J.-C., Allen, R. C., Smith, C. W., Kistler, L. M., Spence, H. E., et al. (2015), The occurrence and wave properties of H^+-, He^+-, and O^+-band EMIC waves observed by the Van Allen Probes. *Journal of Geophysical Research: Space Physics*, 120, 7,477-7,492. doi:10.1002/2015JA021358

Saikin, A. A., Zhang, J.-C., Smith, C. W., Spence, H. E., Torbert, R. B., & Kletzing, C. A. (2016), The dependence on geomagnetic conditions and solar wind dynamic pressure of the spatial distributions of EMIC waves observed by the Van Allen Probes. *Journal of Geophysical Research: Space Physics*, 121, 4,362-4,377. doi:10.1002/2016JA022523

Sakaguchi, K., Shiokawa, K., Ieda, A., Miyoshi, Y., Otsuka, Y., Ogawa, T., Connors, M., Donovan, E. F., & Rich, F. J. (2007), Simultaneous ground and satellite observations of an isolated proton arc at subauroral latitudes. *Journal of Geophysical Research*, 112, A04202. doi:10.1029/2006JA012135

Sakaguchi, K., Kasahara, Y., Shoji, M., Omura, Y.,4, et al. (2013), Akebono observations of EMIC waves in the slot region of the radiation belts. *Geophysical Research Letters*, 40, 5587-5591. doi:10.1002/2013GL058258

Shoji, M., Miyoshi, Y., Omura, Y.,Kistler, L. M., Kasaba, Y., Matsuda, S.,et al. (2018). Instantaneous frequency analysis on nonlinear EMIC emissions: Arase observation. *Geophysical Research Letters*, 45, 13,199-13,205. doi:10.1029/2018GL079765

945 Shoji, M., Miyoshi, Y., Kistler, L.M. et al (2021), Discovery of proton hill in the phase space
946 during interactions between ions and electromagnetic ion cyclotron waves. Science Report, 11,
947 13480. doi:10.1038/s41598-021-92541-0
948
949 Shumko, M. B. Gallardo-Lacourt, A. J. Halford, L. W. Blum, J. Liang et al. (2022), Proton Aurora
950 and Relativistic Electron Microbursts Scattered by EMIC Waves, Front. Astron. Space Sci.,
951 9:975123. doi;10.3389/fspas.2022.975123
952
953 Stix, T. H. (1962), The Theory of Plasma Waves, McGraw-Hill, New York.
954
955 Teng, S., Li, W., Tao, X., Ma, Q., Wu, Y., Capannolo, L., et al. (2019), Generation and
956 characteristics of unusual high frequency EMIC waves. *Geophysical Research Letters*, 46, 14,230-
957 14,238. doi:10.1029/2019GL085220
958
959 Thorne, R. M. (2010), Radiation belt dynamics: The importance of wave-particle interactions.
960 *Geophysical Research Letters*, 37, L22107. doi:10.1029/2010GL044990
961
962 Tsurutani, B. T., et al. (2016), Heliospheric Plasma Sheet (HPS) impingement onto the
963 magnetosphere as a cause of Relativistic Electron Dropouts (REDs) via coherent EMIC wave
964 scattering with possible consequences for climate change mechanisms. *Journal of Geophysical*
965 *Research: Space Physics*, 121, 10,130-10,156. doi:10.1002/2016JA022499
966
967 Tsyganenko, N. A., and Sitnov, M. I. (2005), Modeling the dynamics of the inner magnetosphere
968 during strong geomagnetic storms. *Journal of Geophysical Research*, 110, A03208.
969 doi:10.1029/2004JA010798
970
971 Usanova, M. E., Mann, I. R., Rae, I. J., Kale, Z. C., Angelopoulos, V., Bonnell, J. W., et al.(2008),
972 Multipoint observations of magnetospheric compression-related EMIC Pc1 waves by THEMIS
973 and CARISMA. *Geophysical Research Letters*, 35, L17S25. doi: 10.1029/2008GL034458
974
975 Usanova, M. E., Mann, I. R., Bortnik, J., Shao, L., and Angelopoulos, V. (2012), THEMIS
976 observations of electromagnetic ion cyclotron wave occurrence: Dependence on AE, SYMH, and
977 solar wind dynamic pressure. *Journal of Geophysical Research*, 117, A10218.
978 doi:10.1029/2012JA018049
979
980 Vines, S. K., Allen, R. C., Anderson, B. J., Engebretson, M. J., Fuselier, S. A., Russell, C. T., et
981 al. (2019), EMIC waves in the outer magnetosphere: Observations of an off-equator source region.
982 *Geophysical Research Letters*, 46, 5,707-5,716. doi:10.1029/ 2019GL082152
983
984 Wang, D., et al. (2015), Statistical characteristics of EMIC waves: Van Allen Probe observations.
985 *Journal of Geophysical Research: Space Physics*, 120, 4,400-4,408. doi:10.1002/2015JA021089
986
987 Wang, D., et al. (2016), Geomagnetic storms and EMIC waves: Van Allen Probe observations.
988 *Journal of Geophysical Research: Space Physics*, 121, 6444- 6457. doi:10.1002/2015JA022318.
989

Wang, X. Y., et al. (2017), The occurrence and wave properties of EMIC waves observed by the Magnetospheric Multiscale (MMS) mission. *Journal of Geophysical Research: Space Physics*, 122, 8,228-8,240. doi:10.1002/2017JA024237

Yokota, S., Kasahara, S., Mitani, T. et al. (2017), Medium-energy particle experiments–ion mass analyzer (MEP-i) onboard ERG (Arase). *Earth Planets Space*, 69, 172. doi.10.1186/s40623-017-0754-8

Yue, C., Zong, Q.-G., & Wang, Y. F. (2009), Response of the magnetic field and plasmas at the geosynchronous orbit to interplanetary shock. *Chinese Science Bulletin*, 54. doi: 10.1007/s11434-009-0649-6

Yue, C., Zong, Q.-G., Zhang, H., Wang, Y. F., Yuan, C. J., Pu, Z. Y., et al. (2010), Geomagnetic activities triggered by interplanetary shocks. *Journal of Geophysical Research: Space Physics*, 115, A00I05. doi:10.1029/2010JA015356

Yue, C., Zong, Q., Wang, Y., Vogiatzis, I. I., Pu, Z., Fu, S., & Shi, Q. (2011), Inner magnetosphere plasma characteristics in response to interplanetary shock impacts. *Journal of Geophysical Research: Space Physics*, 116, A11206. doi:10.1029/2011JA016736

Yue, C., Bortnik, J., Chen, L., Ma, Q., Thorne, R. M., Reeves, G. D., & Spence, H. E. (2017a), Transitional behavior of different energy protons based on Van Allen Probes observations. *Geophysical Research Letters*, 44(2), 625-633. doi:10.1002/2016GL071324

Yue, C., Bortnik, J., Thorne, R. M., Ma, Q., An, X., Chappell, C. R., et al. (2017b), The characteristic pitch angle distributions of 1 eV to 600 keV protons near the equator based on Van Allen Probes observations. *Journal of Geophysical Research: Space Physics*, 122, 9,464-9,473. doi.org/10.1002/2017JA024421

Yue, C., Bortnik, J., Li, W., Ma, Q., Gkioulidou, M., Reeves, G. D., et al. (2018), The composition of plasma inside geostationary orbit based on Van Allen Probes observations. *Journal of Geophysical Research: Space Physics*, 123, 6,478-6,493. doi:10.1029/2018JA025344

Yue, C., Jun, C.-W., Bortnik, J., An, X., Ma, Q., Reeves, G. D., et al. (2019), The relationship between EMIC wave properties and proton distributions based on Van Allen probes observations. *Geophysical Research Letters*, 46, 4,070-4,078. doi:10.1029/2019GL082633

Zhou, X, and Tsurutan, B. T. (1999), Rapid intensification and propagation of the dayside aurora: Large scale interplanetary pressure pulses (fast shocks) . *Geophysical Research Letters*, 26(8), 1097-1100. doi:10.1029/1999GL900173